Numerical investigation of nanoparticle deposition in the olfactory region among pediatric nasal airways with adenoid hypertrophy

Zhang, Ya, Hu, Zhenzhen, Wang, Yusheng, Lou, Miao, Ma, Ruiping, Gong, Minjie, Dong, Jingliang, Zheng, Guoxi and Wang, Botao (2023) Numerical investigation of nanoparticle deposition in the olfactory region among pediatric nasal airways with adenoid hypertrophy. Computers in Biology and Medicine, 167. ISSN 0010-4825

Numerical investigation of nanoparticle deposition in the olfactory region among pediatric nasal airways with adenoid hypertrophy

Ya Zhang [a,1], Zhenzhen Hu [a,b,1], Yusheng Wang [a], Miao Lou [c], Ruiping Ma [a], Minjie Gong [a], Botao Wang [a], Jingliang Dong [d,e,*], Guoxi Zheng [a,*]

[a] *Department of Otolaryngology Head and Neck Surgery, The Second Affiliated Hospital of Xi'an Jiaotong University, Xi'an, Shaanxi, 710004, China*
[b] *School of Engineering, RMIT University, Bundoora, VIC, 3083, Australia*
[c] *Department of Otorhinolaryngology Head and Neck Surgery, Shaanxi Provincial People's Hospital, Xi'an, Shaanxi, 710068, China*
[d] *Institute for Sustainable Industries & Liveable Cities, Victoria University, PO Box 14428, Melbourne, VIC, 8001, Australia*
[e] *First Year College, Victoria University, Footscray Park Campus, Footscray, VIC, 3011, Australia*

* Corresponding authors.
E-mail addresses: jingliang.dong@vu.edu.au (J. Dong), zhengguoxi888@sina.com (G. Zheng).
[1] The authors contributed equally to this work.

Abstract

To understand inhaled nanoparticle transport and deposition characteristics in pediatric nasal airways with adenoid hypertrophy (AH), with a specific emphasis on the olfactory region, virtual nanoparticle inhalation studies were conducted on anatomically accurate child nasal airway models. The computational fluid-particle dynamics (CFPD) method was employed, and numerical simulations were performed to compare the airflow and nanoparticle deposition patterns between nasal airways with nasopharyngeal obstruction before adenoidectomy and healthy nasal airways after virtual adenoidectomy. The influence of different inhalation rates and exhalation phase on olfactory regional nanoparticle deposition features was systematically analyzed. We found that nasopharyngeal obstruction resulted in significant uneven airflow distribution in the nasal cavity. The deposited nanoparticles were concentrated in the middle meatus, septum, inferior meatus and nasal vestibule. The deposition efficiency (DE) in the olfactory region decreases with increasing nanoparticle size (1 to 10 nm) during inhalation. After adenoidectomy, the pediatric olfactory region DE increased

significantly while nasopharynx DE dramatically decreased. When the inhalation rate decreased, the deposition pattern in the olfactory region significantly altered, exhibiting an initial rise followed by a subsequent decline, reaching peak deposition at 2 nm. During exhalation, the pediatric olfactory region DE was substantially lower than during inhalation, and the olfactory region DE in the pre-operative models were found to be significantly higher than that of the post-operative models. In conclusions, ventilation and particle deposition in the olfactory region were significantly improved in post-operative models. Inhalation rate and exhalation process can significantly affect nanoparticle deposition in the olfactory region.

Keywords: Olfactory region, Nanoparticle exposure, Virtual surgery, Computational fluid-particle dynamics, Nasal airway

1. Introduction

The nasal cavity is a complex anatomical structure with important physiological functions, including ventilation, heating and humidification, cleaning and filtration, immune defense and olfaction, etc [1]. The olfactory area, located at the uppermost of the nasal cavity, is the sole region in human body where the central nervous system (CNS) is in direct contact with the environment. Air pollution and occupational exposure are probably the two main sources of exposure to airborne nanoparticles. Solid proof indicates that ultrafine particles (nanoparticles) in air pollution can reach the brain through the olfactory pathway, and that this is a key mechanism for the neurodegenerative effects of air pollution [2-4]. Once the toxic nanoparticles reach the brain, a variety of negative effects can be observed, including oxidative stress, inflammation, and neurodegeneration [5,6]. While this route of exposure from the nose to the brain has not been confirmed in humans, it has been proven in non-human primates [7]. As part of the investigation of this potential exposure pathway, it is necessary to quantify the dose of inhaled nanoparticles deposited in the human olfactory region.

Compared to adults, children have smaller nasal cavity volumes, relatively

simpler and immature nasal turbinate structures, and narrower nasopharynges, resulting in a relatively higher proportion of airflow being directed towards the olfactory region [8]. The adenoids, commonly referred to as "nasopharyngeal tonsils," are healthy lymphatic tissues at the roof of the nasopharynx that act as a barrier against upper respiratory illnesses [9]. As reported, 42-70% of children and adolescents experience adenoid hypertrophy (AH), with adenoids typically reaching their maximum size between the ages of 2 and 6 years, after which adenoid tissue gradually regresses [10,11]. AH is associated with decreased appetite and potential growth disturbances, and some affected children may exhibit adenoid facies. Furthermore, AH is also a common etiological factor for olfactory loss in children [12,13]. This is due to the fact that AH can significantly affect nasal airflow and nasal mucosal physiology in children, thereby negatively affecting olfactory function. Adenoidectomy is the most common surgical treatment in the clinic [14]. In fact, subtle variations in nasal anatomical structures can lead to significant differences in odor perception [15]. However, the impact of alterations in airflow and its associated particle transport and deposition characteristics caused by AH on olfactory perception has not yet been fully comprehended. This is of significant importance for therapeutic decisions of adenoidectomy and the improvement of olfactory function. Therefore, there is a great need for a comprehensive understanding of the impact of nasopharyngeal obstruction caused by AH on airflow and nanoparticle transport and deposition characteristics in the pediatric olfactory region.

Currently, some researchers have investigated the airflow distribution and particle deposition characteristics in the nasal cavity of children. Corda et al. [16] conducted a numerical study on the nasal airflow patterns in newborns, infants, and adults, demonstrating that neonates have underdeveloped nasal cavities with the absence of the inferior meatus, resulting in a notably uneven airflow distribution. Cheng et al. [17] investigated the DE within nasal replicas of 1.5-year-old, 2.5-year-old, and 4-year-old children and reported that intranasal deposition decreased with increasing age in the particle size range of 1-200 nm. Golshahi et al. [18] researched the particle deposition with aerodynamic diameters of 0.5 - 5.3 μm in nasal replicas of children aged 4 - 14

years using in vitro experimental methods. Their research demonstrated that particle deposition increased with an increase in particle size and flow velocity, with impaction being the primary deposition mechanism. Zhou et al. [19] performed in vitro experiments and computational fluid dynamics (CFD) analyses of particle deposition (1-20 μm) in the nasal cavity of a 5-year-old child. Results showed that the total deposition from the in vitro experiments and CFD predictions matched to a high degree. Xi et al. [20] evaluated the transport and deposition of aerosols ranging from 0.5 to 32 μm in a nasal-laryngeal airway model of 5-year-old children. The results indicated significant differences between children and adults in the deposition of inhaled aerosols, which should be considered as a factor in the risk assessment of airborne toxicants. Subsequently, the effect of age on intranasal airflow and ultrafine aerosol particle deposition were numerically assessed by Xi et al. [21] in a 10-day-old neonate, a 7-month-old infant, a 5-year-old child, and a 53-year-old adult, and the differences in airway physiology, breathing resistance, and aerosol filtering efficiency among the four models were quantified and compared. Results showed that the nasal–laryngeal airways at different ages, albeit differ significantly in morphology and dimension, do not significantly affect the total deposition fractions or maximum local deposition enhancement for ultrafine aerosols. It is not difficult to find that these previous studies have focused primarily on the nasal cavity among healthy children, or the effects of anatomical and physiological variation between children and adults on particle transport and deposition. There is a significant paucity of research on the nasal cavity of children with pathological changes. Therefore, previous research findings may not be applicable to the nasal airways of children with severe pathological alterations, since any minor lesion can impact nasal airway patency and its associated particle transport and deposition characteristics.

Furthermore, Feng et al. [22] classified 35 children aged 9-15 years into two groups based on their adenoidal nasopharyngeal (AN) ratio (Group 1 with AN ratio $<$ 0.6; Group 2 with AN ratio $\geq$ 0.6) and conducted numerical simulations of the aerodynamic characteristics in their upper airways. The study revealed that the maximum velocity in the nasopharynx was the most sensitive aerodynamic parameter,

and an AN ratio greater than 0.6 may be associated with a significant increase in maximum velocity. Two of our recent articles respectively reported the effect of different degrees of AH on pediatric upper airway aerodynamics and the deposition distribution and influencing factors of Artemisia pollen (21.0 μm) in various anatomical sites of the upper airways of children with AH [23,24]. We found that when the AN ratio is ≥ 0.7, there is a significant flow-limiting effect in the nasopharynx. There are noticeable differences in the deposition hotspots and DE of Artemisia pollen within the nasal cavities between children and adults. The motion and deposition of microparticles are driven by inertia and drag forces, whereas for nanoparticles, it is driven by diffusion resulting from Brownian motion. Due to the different particle motion mechanisms, our previous research findings cannot be applied to nanoparticles. Sun et al. [25] numerically investigated the effect of nasopharyngeal obstruction on the transport and deposition of nanoparticles in the nasal airways of children and reported that the flow field in the nasal cavity was normalised after adenoidectomy, and better nanoparticle transport was obtained in the affected region. However, this study included only one child and did not consider other influencing factors.

Due to ethical concerns and the difficulty in distinguishing particles deposited in the olfactory region from those deposited elsewhere in the nasal cavity, in vivo measurements of olfactory region dosages pose a challenge. Conducting in vitro studies using nasal replicas is also challenging as regional analysis is required to differentiate olfactory region deposition from non-olfactory region deposition. Currently, there is no literature reporting quantitative experiments on nanoparticle deposition in the human olfactory region. However, computational models of airflow and particle transport are an attractive tool for assessing the deposition of nanoparticles in the human olfactory region. Computational Fluid Dynamics (CFD) can be employed to simulate airflow patterns and quantify the dose of inhaled particles deposited in the olfactory region. Therefore, we conducted a virtual nanoparticle inhalation study using CFD, which is needed for the pre-evaluation of surgical outcomes in children with AH.

Quantitative comparisons of airflow and particle deposition characteristics before and after virtual surgery in children with AH can provide deeper insights into the impact

of nasopharyngeal obstruction on olfactory function, thus effectively guiding clinical treatment decisions. To date, research in this area remains limited. In addressing this research gap, this study conducted a detailed comparative analysis from a fluid-particle dynamics perspective on the nasal airways of 4 anatomically precise children with AH and the nasal airways of 4 children after virtual surgery. The effects of inhalation rate and exhalation processes on airflow and nanoparticle deposition in the olfactory region were systematically elucidated. The aim was to provide a scientific basis for evaluating the relationship between nasopharyngeal obstruction and olfactory function, ultimately promoting the improvement of clinical treatment outcomes. For the nasal airways after virtual surgery, there was a significant improvement in ventilation and particle deposition in the olfactory region, suggesting that olfactory loss may be of value in deciding whether to perform adenoidectomy in children with nasopharyngeal obstruction.

2. Methods

2.1. Study subjects

Computed tomography (CT) images (Digital Imaging and Communications in Medicine format, DICOM) of 4 children diagnosed with AH were retrospectively collected. There were 3 males and 1 female with an average age of 4±0.82 years. The CT image resolution was 512 × 512 pixels with a slice interval of 0.5 mm. The AN ratio is defined as the ratio of adenoid thickness to nasopharyngeal width, reflecting both the size of the adenoids and the patency of the nasopharyngeal airway [26]. The reported AN ratio for healthy children is 0.583±0.0741 [27]. In this study, the AN ratio for the four children were 0.86, 0.79, 0.84, and 0.80, with an average AN ratio of 0.82±0.03. The specific measurement method for the AN ratio is detailed in our previous work [23,24]. The study by Adedeji et al. [28] demonstrated that children aged 3-5 years with AH often exhibit severe nasopharyngeal obstruction, with AN ratio ranging from 0.80 to 0.89, indicating the representativeness of the AN ratio in this age range in our study. The children had no obvious abnormalities in the anatomy and morphology of the nasal cavity, and no previous history of severe nasal deformity, nasal trauma, septal perforation, nasal tumors or nasal surgery. This study was authorized by the Institutional

Review Board and Medical Ethics Committee of the Second Affiliated Hospital of Xi'an Jiaotong University (No. 2021-186), and the parents of the children all signed written informed consent form and were completely aware of the pertinent facts and risks.

2.2. Airway reconstruction for pre- and post-operative models

The reconstruction of the pediatric airway structures of interest (facial features, nasal cavity, and larynx) was performed using the free open-source software package, 3D Slicer, from CT images. Since the paranasal sinuses have a neglectable effect on the airflow inside the nasal cavity [29-31], they were excluded from the reconstruction process except for the maxillary sinuses. The specific reconstruction process of the pediatric nasal airways is illustrated in Fig. 1. Each respiratory tract model is connected through the nostrils, forming a continuous pathway from the external space to the end of the larynx. We achieved virtual surgery by adjusting the degree of segmentation of the adenoid region (Fig. 2). Notably, the post-operative model was essentially identical to the pre-operative model, except for the nasopharyngeal obstruction area where virtual surgery was performed. After removing the enlarged adenoid tissue by virtual surgery, the nasopharyngeal airway structure was restored to normal state. A total of 8 models were constructed, including 4 original AH models and 4 health models after virtual surgery (Fig. 3).

All reconstructed models underwent the surface smoothing process, and subsequently, the nasal surface of each model was divided into 10 distinct regions based on anatomical structure and functional considerations (Fig. 4). To accurately capture the unevenly distributed airflow patterns around the nostrils, a hemispherical breathing zone with a radius of 10 cm was created which encompassed the external nose and its surrounding facial regions. Besides, in order to precisely establish airway outflow conditions and to advance numerical stability and convergence, the laryngeal area was additionally preserved.

Specific details of model validation can be found in our previous work [23]. In the previous study, a 1:1 scale model of a child's upper airway was fabricated by three-dimensional stereolithography (STL) technology. Nasal resistance of the 3D printed model was measured (Equipment Model NR6, GM Instruments) and compared the

measurements with numerical results. The results showed that there was a positive correlation between pressure drop and flow rate regardless of experimental measurement or numerical simulation. The experimental data exhibited good agreement with the numerical results, confirming the reliability of the numerical model.

With the advancement of CT scanning technology, we can obtain authentic and accurate image data [32]. These data are acquired from clinical scans of actual children to ensure that the anatomical structures of the models match those of real children. The nature of our work as otolaryngologists makes us very aware of the anatomical structures and characteristics of the nasal cavity. This allows us to accurately remove unneeded structures and preserve the target airway of interest. Furthermore, our previous work [23] performed nasal resistance measurements on 3D-printed pediatric models and compared them with numerical results. The findings indicated a strong agreement between experimental and numerical results, further confirming the reliability of our model. However, there are individual differences in the shape and size of the pediatric nasal cavity, and as such, our model may not cover anatomical variations in all children. The accuracy of the model is limited by the resolution of the CT scans, and fine structures may not be fully reproduced in the model.

2.3. Mesh Generation

ANSYS Fluent Meshing (ANSYS, Inc., Canonsburg, Pennsylvania, USA) was employed to generate polyhedral meshes with mesh sizes ranging from 0.05 to 0.3 mm. Five layers of highly dense prism mesh were attached to the nasal wall to resolve the viscous flow characteristics at the near-wall surface (Fig. 5). The first prism layer was set to 0.02 mm and the growth rate was 1.1. Compared to traditional tetrahedral mesh, polyhedral mesh prevails in all aspects, such as improved numerical convergence, reduced susceptibility to stretching, and higher calculation efficiency [33]. After the grid independence tests incorporating coarse, medium and fine mesh numbers, the final mesh numbers of all pre- and post-operative models were 2.0-2.2 million, achieving a balance between computational efficiency and accuracy.

2.4. Boundary conditions

During inhalation, the hemisphere of the breathing zone was defined as the

"pressure inlet" with zero-gauge pressure, and the outlet of the model was defined as the "velocity outlet", and the velocity magnitude was calculated by dividing the volumetric flow by the outlet area (Fig. 6A). Tidal volumes and respiratory rates for children of different ages were obtained from data reported by Hofmann [34]. 2.7s was set as one breathing cycle in this study [35]. The calculated inhalation flowrates of 3 to 5 years old children were 7.84, 9.03 and 9.77 L/min, respectively, which can satisfy the resting state. Table 1 shows the literature-based, quiet-breathing respiratory parameters. Under low-flow inhalation conditions (flow rate halved), the inhalation flowrates were set to 3.92, 4.52, and 4.89 L/min, respectively. During exhalation, the outlet of the airway model was set as the "velocity inlet" and the respiratory hemisphere was defined as the "pressure outlet" with zero-gauge pressure (Fig. 6B). The velocity value was calculated based on volume flow and outlet area. The boundary condition for the particle-wall interaction was set as "trapped wall," indicating that the inhaled particles would deposit at initial contact with the airway surface. Non-slip, stationary wall boundary conditions were applied to the face and nasal surfaces. The inhaled airflow was assumed to be stable and incompressible.

2.5. Airflow simulation

The k-ω SST model was applied to solve the unique aerodynamic characteristics of the pediatric nasal airway. The incompressible Navier-Stokes equation was determined to be the control equation, and the Second Order Upwind algorithm was used to calculate the nasal cavity airflow during steady-state inhalation. The pressure-velocity coupling was handled through the SIMPLE method. ANSYS Fluent 2021 R1 software (ANSYS, Inc., Canonsburg, Pennsylvania, USA) was applied to solve the correlated algebraic equations, and the governing equations were discretized using the finite volume approach.

2.6. Particle tracking

The one-way coupled Lagrangian approach was implemented for a dispersed phase with low volume fraction (nanoparticles in present study). This method involves simulating the airflow field first and then tracking the trajectories of individual particles by integrating the particle force balance equation. The drag force, gravity, and

Brownian force were all taken into consideration:

$$\frac{du_i^p}{dt} = F_D + F_G + F_B \quad (1)$$

where u_i^p is the particle velocity, F_D is the drag force per unit particle mass described as:

$$F_D = \frac{18\mu\left(u_i^{\mathrm{g}} - u_i^{\mathrm{p}}\right)}{C_c d_p^2 \rho_p} \quad (2)$$

where u_i^g is the airflow velocity, μ is the air viscosity, d_p is the particle diameter, ρ_p is the particle density, and C_{c} is the Cunningham correction factor given by:

$$C_c = 1 + \frac{2\lambda}{d_p}\left(1.257 + 0.4e^{-\frac{1.1d_p}{2\lambda}}\right) \quad (3)$$

where λ is the air molecular mean free path, assumed to be 67nm.

Brownian force (F_B) is of the form $\xi_i\sqrt{(\pi S_o)/\Delta t}$, where ξ_i are zero-mean, unit-variance-independent Gaussian random numbers, and Δt is the particle integration time-step. S_o is a spectral intensity function:

$$S_{\mathrm{o}} = \frac{216\nu k_B T}{\pi^2 \rho d_p^5 \left(\frac{\rho_p}{\rho}\right)^2 C_c} \quad (4)$$

In present study, the nanoparticles were assumed to be spherical shapes with a particle density (ρ_p) of 1000 kg/m^3 and the air density (ρ) was set to 1.225 kg/m^3. ν is the kinematic viscosity, T is the Kelvin temperature of inhaled air (in this case 300 K), k_B is the Boltzmann constant, and C_c is the Cunningham correction factor. The simulated particle diameter ranges from 1 to 10 nm with 1nm incrementation. During inhalation, for each particle size, 100,000 particles were released uniformly from a spherical surface (3 cm in radius) centered on the nose tip, which completely encompasses the nasal cavity and its surrounding facial area (Fig. 6A). Once the nanoparticles entered the nasal cavity, Fluent's Discrete Phase Model (DPM) mode was used to track them until the particles were "trapped" by the nasal airway mucosa or particles outflew the airway. In fact, what we refer to as "taste" refers to the stimulating effect of food volatiles on olfactory epithelial cells when food fragments pass through

the nasopharynx during mastication and deglutition [36]. Therefore, during exhalation, a cross-section was set up in the nasopharynx from which nanoparticles were uniformly and passively released to mimic nanoparticle transport and deposition during exhalation (Fig. 6B). In the exhalation process, we primarily observed the particle deposition within the olfactory region, without further analysis of particle deposition in other anatomical regions of the nasal cavity. Since the mucus layer covers the surface of the nasal airway, particle deposition was considered to occur when the particles strike the surface of the nasal airway, and therefore rebound was not taken into account.

2.7. Statistical analysis

Statistical analysis was performed using SPSS 21.0 software. The differences in particle deposition before and after surgery, at different inhalation rates, and separately in inhalation and exhalation were compared by paired t-test. Differences were considered statistically significant when $P< 0.05$.

3. Results

3.1. Airflow analysis

The results of this study are schematically represented by nasal model B. The distribution of airflow streamlines in the pre- and post-operative models during inhalation and exhalation is shown in Fig. 7. Overall, the airflow streamlines of the two nasal airway models during inhalation were mainly distributed in the inferior and middle meatus, with less airflow entering the anterior upper part of the nasal cavity. Specifically, the AH model showed sudden airflow acceleration near the nasopharyngeal obstruction site, with peak velocity up to 5.17 m/s. Compared with the AH model, the local peak velocity in the nasopharynx of the post-operative model was about 2.21 m/s, which is only about 43% of the obstructed airway in the nasopharynx. At the same time, the airflow streamlines in the post-operative model were more dispersed, with more streamlines entering the upper part of the nasal cavity. During exhalation, the airflow streamlines of both nasal airway models were predominantly distributed in the inferior and middle meatus, with a relatively more airflow entering the anterior upper part of the nasal cavity. Obvious vortex formation can be seen at the olfactory region of the post-operative models. Compared with the inhalation phase, peak velocities in the nasopharynx were increased in both models during exhalation,

and were especially pronounced in the post-operative model (increased by 117%).

Fig. 8 shows the flow patterns at the olfactory interface (an artificial location at the bottom of the olfactory region used to extract velocity data) for pre- and post-operative models during inhalation and exhalation phases. These results directly reflect the ventilation status of the olfactory region. During inhalation, relatively limited airflow entered the olfactory region of the pre-operative model, with a peak local velocity of 1.19 m/s occurring at the posterior end of the left chamber. The olfactory ventilation status was slightly improved in the post-operative model, with a peak local velocity of 1.71 m/s observed at the posterior end of the left chamber side. During exhalation, the flow patterns at the olfactory interface experienced abrupt changes in both direction and magnitude. Specifically, the pre-operative model exhibited a predominant anterior-to-posterior flow direction with a local peak velocity of 1.93 m/s in the left chamber. In contrast, the post-operative model displayed a posterior-to-anterior flow direction with a local peak velocity of 2.59 m/s in the left chamber.

3.2. Model validation

To validate the accuracy of our models, the DE (mean ± standard deviation) of 1-10 nm particles from the current models of 8 children was compared with pediatric deposition data from the published literature. An in vitro nasal replica of a 4-year-old child by Cheng et al. [17] and a nasal model of a 5-year-old child by Xi et al. [21], both of which were similar in age to our children, were used for data comparison. Cheng et al. [17] measured the DE of monodisperse NaCl or Ag aerosols (0.0046-0.20 μm) in pediatric nasal casts at respiratory flow rates of 3, 7, and 16 L/min. The nasal cast extended from the nasal tip to the junction of the nasopharynx and pharynx, and monodisperse aerosols were released from the nostril entrance. Xi et al. [21] numerically simulated the transport and deposition of 1-100 nm particles in a child's nose-throat model under conditions ranging from resting to vigorous activity (i.e., 2-45 L/min). Ultrafine particles were introduced into the nasal cavity from the nostril inlet plane.

As can be observed from Fig. 9, our pre- and post-operative models showed slight changes in particle DE due to nasopharyngeal obstruction. Specifically, the nasopharyngeal obstructed model showed a slightly higher DE, while slightly fewer nanoparticles were deposited in the model that underwent virtual surgery. Overall, our current models agreed well with the deposition results of the Xi et al. [21] for most particle sizes. Compared to the in vitro experimental measurements by Cheng et al.

[17], our models had a similar deposition trend with a relatively low DE. This variation is largely attributable to differences in respiratory flow rates and exposure patterns. The higher inhalation flow rate (7.8-10 L/min) in our models resulted in a lower DE of nanoparticles, for which diffusion plays a dominant role. Unlike the inhalation environment of our models, the models of Xi et al. [21] and Cheng et al. [17] did not include an outside hemispherical breathing zone, and the nostrils were directly connected to the uniformly released aerosol. As a result, more particle deposition was observed in the nasal airways, especially diffusion-dominated particles. In addition, other factors contributing to the variability of the available data could be anatomical differences between subjects, as well as nanoparticle aggregation in the experiments.

3.3. Nasal cavity particle deposition during inhalation

The following equation was applied to calculate the DE of each anatomical region: DE=local deposition particle number /total released particle number × 100%. Escape rate=number of particles escaping from larynx /total released particle number × 100%. The total DE of nanoparticles in the pre- and post-operative models are shown in Fig. 10. The total DE gradually decreases with the increase of nanoparticle sizes due to the diminished particle diffusion effect. Pre- and post-operative models showed the same depositional trend. The total DE peaked for highly diffuse 1nm particles at 72.67%±5.26% and 70.01%±4.89% pre- and post-operatively, respectively; whereas it dropped to the minimum for 10 nm particles at 9.35%±1.41% and 8.54%±1.33% pre- and post-operatively, respectively. In addition, the total DE was reduced in the post-operative models compared to the pre-operative models ($t=7.122$, $p=0.000$). Two particle sizes, 1 nm and 10 nm, were selected as representative particle sizes, and their spatial deposition patterns are shown in Fig. 11. Overall, 1 nm particles had a stronger diffusion effect and therefore a higher overall DE (around 70%-73%). In contrast, for 10 nm particles, the overall DE was significantly lower to 8.5%-9.5% due to significantly weaker particle diffusion.

The DE of nanoparticles in each anatomical site of the model before and after surgery is shown in Fig. 12. 1-10 nm particles were mainly deposited in the middle meatus, septum, inferior meatus and nasal vestibule in the nasal cavity. The DE decreased with increasing nanoparticle size in all anatomical sites except the maxillary sinus. Deposition trends were similar between the pre- and post-operative models. After adenoidectomy, the DE in the nasopharynx was significantly lower in children ($t=6.335$, $p=0.000$). On the contrary, the escape rate of nanoparticles at the outlet gradually

increased with increasing particle size (Fig. 13). The escape rate at the outlet was higher in the post-operative models than that in the pre-operative models (t=-9.200, p=0.000).

3.4. Olfactory region particle deposition during inhalation

The DE of nanoparticles in the olfactory region of the model before and after surgery is shown in Fig. 14. The DE in the olfactory region decreased with increasing nanoparticle sizes during resting inhalation. Deposition trends were similar between the pre- and post-operative models, with the olfactory region DE peaked for the smallest 1 nm particles (2.33%±2.04% vs 2.78%±2.04%), while the olfactory region DE was minimum for the largest 10 nm particles (0.25%±0.16% vs 0.27%±0.12%). In addition, the olfactory region nanoparticle DE of the post-operative models was generally higher than that of the pre-operative models (t= -2.538, p=0.032).

When the inhalation flow rate was reduced (flow rate halved), the deposition trend in the olfactory region was altered significantly, showing an initial rise followed by a subsequent decline trend. For highly diffuse 1 nm particles, olfactory region DE was significantly reduced both before and after surgery (1.42%±1.35% vs 1.70%± 1.48%); whereas for 2 nm particles, the olfactory region DE peaked (1.98%±1.27% vs 2.28%±1.53%). For particles sized 1-6 nm, the olfactory region DE of the post-operative models was higher than that of the pre-operative models, whereas 7-10 nm particles showed almost the same DE in the pre- and post-operative olfactory regions. The olfactory region DE of 2-10 nm particles generally increased when the inhalation flow rate was halved compared to resting inhalation; and the DE gradually decreased with increasing particle size.

3.5. Olfactory region particle deposition during exhalation

The direction of the exhalation airflow is not simply the opposite of that of the inhalation. The airflow during exhalation was closer to the side of head causing by the shape of the nasopharynx and the back of the turbinate. In order to gain a comprehensive understanding of the factors affecting the nanoparticle DE in the olfactory region, we analyzed the deposition of nanoparticles in the olfactory region during exhalation.

As shown in Fig. 15, the deposition trend of nanoparticles in the olfactory region of children during exhalation was similar to that during inhalation. For particles in the range of 1-10 nm, the DE in the olfactory region decreased gradually with increasing particle sizes. The olfactory region DE of the smallest 1 nm particles peaked at 1.56%±1.08% and 0.63%±0.32% for the pre- and post-operative models, respectively;

whereas the olfactory region DE of the largest 10 nm particles decreased to the minimum (approaching to 0), with 0.09%±0.11% and 0.02%±0.03% for the pre- and post-operative models, respectively. The DE of nanoparticles in the children's olfactory region was generally reduced during exhalation compared to the inhalation phase (t=4.396, p=0.002; t=3.991, p=0.003), with the most pronounced reduction observed in 1 nm particles (less than 1.6%). In addition, the gap between the DEs of the olfactory region in the pre- and post-operative models during exhalation increased further, especially in the post-operative models, where the DE in the olfactory region was generally at its lowest level. Notably, unlike the deposition pattern during inhalation, the olfactory region DE of the pre-operative models was significantly higher compared to the post-operative models during exhalation (t=4.270, p=0.002). Overall, the overall DE in the children's olfactory region was very low (less than 3%) in all of our considered scenarios.

4. Discussion

The morphology of the nasopharynx was significantly altered before and after adenoid surgery, and this resulted in significant changes in nasal airflow dynamics. For the models with AH, the local airflow velocity at the nasopharyngeal obstructed region during inhalation could reach 5.17 m/s. Due to the obvious airflow limiting effect of the nasopharyngeal obstruction area, it is expected that the children will have to exert considerable effort to maintain normal respiratory activity. In the post-operative models, the abnormal airflow dynamics changes in the nasopharynx disappeared, and the local peak velocity was significantly reduced (2.21 m/s), which could alleviate the uncomfortable symptoms of the children to a certain extent. This is consistent with the authors' previous findings [23]. This relationship between the morphology and aerodynamics of the airway can be explained by the Bernoulli effect [37], which states that as the fluid travels through a narrowing portion of a tube, the increase in the velocity of the fluid corresponds with the reduction in pressure. On exhalation, the peak velocity at nasopharyngeal obstruction site in the pre-operative model increased further (5.69 m/s), exacerbating the degree of dyspnea among children, and mouth breathing may occur. This high speed was mainly due to the inherited upstream jet flow (the narrowest area within the pharynx). During inhalation and exhalation, the olfactory region airflow velocity of the post-operative models was significantly higher than that of the pre-operative models, which may be related to the fact that the removal of the

nasopharyngeal obstruction led to an increase in airflow into this region.

The total DE in the nasal cavity decreases gradually with increasing nanoparticle sizes (1-10 nm). Overall, the diffusion effect of 1 nm particles was stronger and therefore the total DE in the nasal cavity was higher. The same deposition trend was reported by Sun et al. [25] in a study of nanoparticle deposition in the nasal cavity of a 3-year-old child. In addition to particle sizes, nasopharyngeal obstruction has an indispensable effect on local DEs alterations in the nasal cavity. More nanoparticles are deposited in the nasopharynx due to the presence of AH. This is due to the fact that for the untreated models with severe obstruction in the nasopharynx, the airflow is significantly accelerated and becomes fully turbulent, preventing Brownian diffusion from occurring. For models after virtual surgery, however, the particle diffusion effect plays the dominant role. Lou et al. [38] have also noted that AH may lead to the accumulation of allergen (e.g., dust, pollen) particles in the nasal cavity and nasopharynx, which can exacerbate the symptoms and duration of allergic rhinitis. However, because the nasopharyngeal obstruction site is located downstream of the nasal airway, the number of particles captured by the main nasal cavity are relatively unaffected, and thus there is less variability in the DE within the main nasal cavity, although particles deposited in the post-operative models are more dispersed.

The DE in the olfactory region of children during resting inhalation decreased with increasing nanoparticle sizes, mainly due to a gradual weakening of the particle diffusion effect. Studies by Dong et al. [39,40] have also reported that for 1 nm particles, the highest deposition dose in the olfactory region was found in the adult model, whereas no significant olfactory region deposition was found for 10 nm particles. In addition, we found that the deposition intensity in the olfactory region between the pre- and post-operative models was significantly different. This is due to the flow-limiting effect of the nasopharyngeal obstruction, which restricts most of the airflow in the pre-operative model to the middle and inferior meatus, with ventilation in the upper part of the nasal cavity being greatly compromised. In contrast, surgical removal of the nasopharyngeal obstruction resulted in a more even distribution of airflow in the model, with more airflow into the upper part of the nasal cavity, resulting in improved ventilation of the olfactory region and superior meatus. Particle deposition in the olfactory region of the post-operative model was significantly enhanced due to improved ventilation of the olfactory region. A clinical study by Fornazieri et al. [41] similarly demonstrated significant improvement in olfactory function after

adenoidectomy in children with pre-operative nasopharyngeal obstruction greater than 50%.

The main deposition mechanism of nanoparticles is diffusion. At lower flow rates, the smaller the particle sizes, the more it is deposited [17]. In present study, it was found that when the inhalation flow rate was reduced (3.92-4.89 L/min), the largest deposited dose in the olfactory region of children corresponded to a particle size of 2 nm rather than at 1 nm, showing an initially increasing and then decreasing deposition trend. This is mainly because the olfactory region was located at the upper posterior part of the nasal cavity and the consideration of inhalation exposure environment of our models. As a result, 1 nm particles with the strongest diffusion effect tend to incur more deposition losses as they pass through the hemispherical breathing zone outside the model and the anterior part of the nasal cavity when the inhalation flow rate is significantly reduced. As a result, the olfactory region deposition intensity of 1 nm particles was observed to be relatively small. In general, the overall DEs in the pediatric olfactory region were very low (<3%), which is related to the deep location of the olfactory region and the fact that most of the inhaled aerosol particles were captured by the anterior nose. Garcia et al. [42] studied the deposition of nanoparticles in the nasal cavity of adults with inhalation rates of 15-30 L/min and reported that olfactory dose of inhaled nanoparticles is highest for 1-2 nm particles, with approximately 1% of inhaled particles deposited in the olfactory region. The main reason for this difference in deposition may be related to differences in the anatomical structure of the nasal cavity and differences in inhalation flow rates between children and adults.

Ingham [43] reported that the diffusion parameter ($\Delta=L/Pe\cdot d_c$) can be introduced to quantify nanoparticle deposition, where L indicates the characteristic length, and d_c stands for the characteristic diameter of the nasal airway. Pe is of the form d_cU/D, U denotes the characteristic airflow velocity, and D stands for the molecular diffusivity of particles in the air. During inhalation, the length coverage of effective flow in the post-operative olfactory region was broader than that pre-operation (as depicted in Fig. 7, in the left side of the pre-operative model, the velocity fields approach zero at the interface of the olfactory region), so the characteristic length (L) of nanoparticle exposure was longer, and the diffusion effect of nanoparticle was enhanced.

During exhalation, the deposition trend in the children's olfactory region was similar to that of the inhalation period, but the DE in the olfactory region was significantly lower. This is due to the L of the olfactory exposure scenario during

exhalation is essentially the same before and after surgery (as depicted in Fig. 7, velocity fields are well above 0.3 m/s at the interfaces of the olfactory region in both models), and the determining factor becomes the characteristic airflow velocity (U). The U in the olfactory region was significantly higher during exhalation than during inhalation, resulting in a significantly weaker diffusion effect of nanoparticles. In particular, the U of the post-operative olfactory region increased dramatically, so that its DE was significantly lower than that of the pre-operative olfactory region. It is worth noting that the changes in flow direction along the olfactory interface are attributed to the presence of the sagittal flow recirculation (Fig. 7). Flow recirculation patterns are generally reduced in the post-operative model, as the length coverage of the bulk flow direction along the interface (anterior-to-posterior for inhalation, posterior-to-anterior for exhalation) is generally longer than in the pre-operative model. This demonstrates that the post-operative model achieves better rearranged flow patterns with reduced flow recirculation in the superior olfactory regions.

In general, the impact of nasopharyngeal obstruction resulting from AH on olfactory function has received little attention from clinicians. Through a comparative study of airflow-particle dynamics before and after surgery in children with AH, we observed that ventilation and particle deposition in the olfactory region were significantly improved after adenoidectomy. This discovery contributes to a better determination of the necessity and optimal timing of surgery for physicians, which is crucial for the healthy growth and improved quality of life in children. Understanding the deposition patterns of nanoparticles contributes to the development of more effective pollutant prevention and control measures, thereby reducing the likelihood of environmental toxin exposure in the olfactory region of children. Furthermore, our model can be utilized for postoperative monitoring, aiding physicians in assessing the degree of surgical success and the recovery status of children's olfactory senses. This facilitates treatment plan adjustments, optimizes patient care, and ensures the best possible recovery outcomes. The findings of this study may hold potential value for the design and optimization of drug delivery systems. By gaining insights into the deposition characteristics of nanoparticles within the nasal airways of children, improvements can be made to nasal drug delivery systems to more effectively transport drugs to the olfactory region.

This study provides a detailed methodology description, including data collection, model construction, parameter settings, boundary conditions, and the principles of

airflow-particle dynamics, sufficient to ensure that other researchers can replicate the study using the same approach. Furthermore, our research findings are consistent with previous relevant studies, which further support the replicability of our research. Other researchers can refer to these related studies to validate our findings. In summary, our study was conducted using standardized methods, which ensures the credibility and replicability of our research.

The study also has some limitations. Firstly, this study focused on children with AH aged 3-5 years, a small age range and a limited sample size. Future studies need to continue to expand the sample size and use more realistic nasal airway models at larger age spans to further confirm these findings. Second, the widely used assumption of stable airflow may have slight impact on the results. In realistic human bodies, the nasal cavity airflow incorporate acceleration and deceleration of a wide range of flow rates, it is not always stable. Shi et al. [44] demonstrated that cumulative effects lead to the changed of particle concentration fields and compared with steady flow status, the cyclic airflow has more inhaled nanoparticles closer to the posterior nasal cavity during deceleration phase, resulting a higher nanoparticle concentration. Jiang and Zhao [45] claimed that despite such differences between steady and cyclic airflows, the steady assumption of the nasal airflow field is still valid over 70% of the cycle period, and the averaged nanoparticle deposition results during breathing cycles can be estimated based on steady cases using empirical correlations, which greatly reduces the computational costs. We analyzed the effects of different inhalation rates and exhalation process on nanoparticle deposition in the olfactory region. Future research can further investigate the mechanisms underlying these effects, particularly the physical and biological mechanisms of nanoparticle deposition in the olfactory region. In addition to inhalation rate and exhalation process, other factors such as age, gender, and disease status may also influence airflow and particle deposition in the olfactory region. Future research can undertake a more comprehensive multi-factor analysis.

5. Conclusion

In this study, a detailed comparative study of the nasal airways before and after virtual surgery in anatomically precise children with AH was performed from the perspective of fluid-particle dynamics. The comprehensive impact of surgical excision, inhalation rate, and exhalation process on airflow and nanoparticle deposition in the olfactory region was systematically elucidated. The results indicate that after

adenoidectomy, the nasopharyngeal morphology returns to normal, and the airflow distribution within the nasal cavity becomes more uniform. For the nasal airways after virtual surgery, there was a significant improvement in ventilation and particle deposition in the olfactory region, suggesting that olfactory loss may be of value in deciding whether to perform adenoidectomy in children with nasopharyngeal obstruction. When the inhalation rate decreased, the deposition intensity of 2-10 nm particles in the olfactory region significantly increased. During exhalation, the deposition intensity in the olfactory region noticeably decreased. The results of this study are expected to provide a scientific basis for adenoidectomy planning and protection against pollutant exposure in the olfactory region, thereby promoting improvements in clinical treatment outcomes and the healthy growth of children. Due to variability among different individuals, future research may require the analysis of deposition characteristics in a larger number of pediatric subjects to continuously validate these findings.

Declaration of competing interest

The authors declare that they have no known competing financial interests or personal relationships that could have appeared to influence the work reported in this paper.

Author contribution to study

Ya Zhang: Conceptualization, Methodology, Validation, Formal analysis, Writing - original draft, auditing, Funding acquisition. **Zhenzhen Hu:** Conceptualization, Methodology, Formal analysis, Writing - review & editing, auditing. **Yusheng Wang:** Datacuration, Visualization, Supervision, Methodology. **Miao Lou:** Software, Validation, Investigation. **Ruiping Ma:** Supervision, Visualization, Methodology. **Minjie Gong:** Project administration, Validation, Methodology. **Botao Wang:** Project administration, Supervision, Validation, Funding acquisition. **Jingliang Dong:** Conceptualization, Methodology, Validation, Formal analysis, Writing - review & editing, Funding acquisition. **Guoxi Zheng:** Conceptualization, Methodology, Validation, Formal analysis, Writing - review & editing, Funding acquisition.

Acknowledgements

This research was funded by the National Natural Scientific Foundation of China (grant number 82000960), the Universities Co-funded Project of Key Research and Development Project of Shaanxi Province (grant number 2020GXLH-Y-017), the Science and Technology Planning Project of Yulin City (grant number CXY-2020-047), and the Australian Research Council (grant number DE210101549).

References

[1] D. Elad, M. Wolf, T. Keck, Air-conditioning in the human nasal cavity, Respir. Physiol. Neurobiol. 163 (2008) 121-127, https://doi.org/10.1016/j.resp.2008.05.002.

[2] M.L. Block, L. Calderon-Garciduenas, Air pollution: mechanisms of neuroinflammation and CNS disease, Trends Neurosci. 32 (2009) 506-516, https://doi.org/10.1016/j.tins.2009.05.009.

[3] L. Calderon-Garciduenas, B. Azzarelli, H. Acuna, R. Garcia, T.M. Gambling, N. Osnaya, S. Monroy, T.M. DEL, J.L. Carson, A. Villarreal-Calderon, B. Rewcastle, Air pollution and brain damage, Toxicol. Pathol. 30 (2002) 373-389, https://doi.org/10.1080/01926230252929954.

[4] L. Calderon-Garciduenas, A.C. Solt, C. Henriquez-Roldan, R. Torres-Jardon, B. Nuse, L. Herritt, R. Villarreal-Calderon, N. Osnaya, I. Stone, R. Garcia, D.M. Brooks, A. Gonzalez-Maciel, R. Reynoso-Robles, R. Delgado-Chavez, W. Reed, Long-term air pollution exposure is associated with neuroinflammation, an altered innate immune response, disruption of the blood-brain barrier, ultrafine particulate deposition, and accumulation of amyloid beta-42 and alpha-synuclein in children and young adults, Toxicol. Pathol. 36 (2008) 289-310, https://doi.org/10.1177/019 2623307313011.

[5] L. Calderon-Garciduenas, R. Torres-Jardon, R.J. Kulesza, S.B. Park, A. D'Angiulli, Air pollution and detrimental effects on children's brain. The need for a multidisciplinary approach to the issue complexity and challenges, Front. Hum. Neurosci. 8 (2014) 613, https://doi.org/10.3389/fnhum.2014.00613.

[6] Y. Liu, Y. Gao, Y. Liu, B. Li, C. Chen, G. Wu, Oxidative stress and acute changes in murine brain tissues after nasal instillation of copper particles with different sizes, J. Nanosci. Nanotechnol. 14 (2014) 4534-4540, https://doi.org/10.1166/jnn.2014.8290.

[7] D.C. Dorman, M.F. Struve, B.A. Wong, J.A. Dye, I.D. Robertson, Correlation of Brain Magnetic Resonance Imaging Changes with Pallidal Manganese Concentrations in Rhesus Monkeys Following Subchronic Manganese Inhalation, Toxicol. Sci. 92 (2006) 219–227, https://doi.org/10.1093/toxsci/kfj209.

[8] J. Dong, Q. Sun, Y. Shang, Y. Zhang, L. Tian, J. Tu, Numerical comparison of inspiratory airflow patterns in human nasal cavities with distinct age differences, Int. J. Numer. Method Biomed. Eng. 38 (2022) e3565, https://doi.org/10.1002/cnm.3565.

[9] P.B. van Cauwenberge, L. Bellussi, A.R. Maw, J.L. Paradise, B. Solow, The adenoid as a key factor in upper airway infections, Int. J. Pediatr. Otorhinolaryngol. 32 (1995) S71-S80, https://doi.org/10.1016/0165-5876(94)01146-o.

[10] L. Pereira, J. Monyror, F.T. Almeida, F.R. Almeida, E. Guerra, C. Flores-Mir, C. Pacheco-Pereira, Prevalence of adenoid hypertrophy: A systematic review and meta-analysis, Sleep. Med. Rev. 38 (2018) 101-112, https://doi.org/10.1016/j.smrv.2017.06.001.

[11] M.F. Evcimik, M. Dogru, A.A. Cirik, M.I. Nepesov, Adenoid hypertrophy in children with allergic disease and influential factors, Int. J. Pediatr. Otorhinolaryngol. 79 (2015) 694-697, https://doi.org/10.1016/j.ijporl.2015.02.017.

[12] A. Altundag, M. Salihoglu, M. Cayonu, H. Tekeli, Clinical assessment of olfactory functions in children who underwent adenotonsillectomy during pre- and post-operative period, Int. J. Pediatr. Otorhinolaryngol. 78 (2014) 1138-1142, https://doi.org/10.1016/j.ijporl.2014.04.032.

[13] I. Konstantinidis, S. Triaridis, A. Triaridis, I. Petropoulos, K. Karagiannidis, G. Kontzoglou,

How do children with adenoid hypertrophy smell and taste? Clinical assessment of olfactory function pre- and post-adenoidectomy, Int. J. Pediatr. Otorhinolaryngol. 69 (2005) 1343-1349, https://doi.org/10.1016/j.ijporl.2005.03.022.
[14] B.S. Turkoglu, E. Aydin, Adenoidectomy: current approaches and review of the literature, Kulak. Burun. Bogaz. Ihtis. Derg. 26 (2016) 181-190, https://doi.org/10.5606/kbbihtisas.2016.32815.
[15] S. Heilmann, G. Strehle, K. Rosenheim, M. Damm, T. Hummel, Clinical assessment of retronasal olfactory function, Arch. Otolaryngol. Head Neck Surg. 128 (2002) 414-418, https://doi.org/10.1001/archotol.128.4.414.
[16] J.V. Corda, B.S. Shenoy, K.A. Ahmad, L. Lewis, P. K, S. Khader, M. Zuber, Nasal airflow comparison in neonates, infant and adult nasal cavities using computational fluid dynamics, Comput. Methods Programs Biomed. 214 (2022) 106538, https://doi.org/10.1016/j.cmpb.2021.106538.
[17] Y.S. Cheng, S.M. Smith, H.C. Yeh, D.B. Kim, K.H. Cheng, D.L. Swift, Deposition of ultrafine aerosols and thoron progeny in replicas of nasal airways of young children, Aerosol Sci. Tech. 23 (1995) 541-552, https://doi.org/10.1080/02786829508965336.
[18] L. Golshahi, M.L. Noga, R.B. Thompson, W.H. Finlay, In vitro deposition measurement of inhaled micrometer-sized particles in extrathoracic airways of children and adolescents during nose breathing, J. Aerosol Sci. 42 (2011) 474-488, https://doi.org/10.1016/j.jaerosci.2011.04.002.
[19] Y. Zhou, J. Xi, J. Simpson, H. Irshad, Y.S. Cheng, Aerosol deposition in a nasopharyngolaryngeal replica of a 5-year-old child, Aerosol Sci. Tech. 47 (2013) 275-282, https://doi.org/10.1080/02786826.2012.749341.
[20] J. Xi, X. Si, J.W. Kim, A. Berlinski, Simulation of airflow and aerosol deposition in the nasal cavity of a 5-year-old child, J. Aerosol Sci. 42 (2011) 156-173, https://doi.org/10.1016/j.jaerosci. 2010.12.004.
[21] J. Xi, A. Berlinski, Y. Zhou, B. Greenberg, X. Ou, Breathing resistance and ultrafine particle deposition in nasal-laryngeal airways of a newborn, an infant, a child, and an adult, Ann. Biomed. Eng. 40 (2012) 2579-2595, https://doi.org/10.1007/s10439-012-0603-7.
[22] X. Feng, Y. Chen, W. Cai, S.A. Lie, K. Hellen-Halme, X.Q. Shi, Aerodynamic characteristics in upper airways among orthodontic patients and its association with adenoid nasopharyngeal ratios in lateral cephalograms, Bmc. Med. Imaging. 21 (2021) 127, https://doi.org/10.1186/s12880-021-00659-4.
[23] Z. Hu, J. Dong, M. Lou, J. Zhang, R. Ma, Y. Wang, M. Gong, B. Wang, Z. Tong, H. Ren, G. Zheng, Y. Zhang, Effect of different degrees of adenoid hypertrophy on pediatric upper airway aerodynamics: a computational fluid dynamics study, Biomech. Model. Mechanobiol. 22 (2023) 1163-1175, https://doi.org/10.1007/s10237-023-01707-4.
[24] Z. Hu, R. Ma, Y. Wang, M. Lou, M. Gong, B. Wang, G. Zheng, J. Dong, Y. Zhang, Quantitative study of Artemisia pollens deposition in the upper airways of children with adenoidal hypertrophy, J. Aerosol Sci. 172 (2023) 106191, https://doi.org/10.1016/j.jaerosci.2023.106191.
[25] Q. Sun, J. Dong, Y. Zhang, L. Tian, J. Tu, Numerical study of the effect of nasopharynx airway obstruction on the transport and deposition of nanoparticles in nasal airways, Exp. Comput. Multiph. Flow. 4 (2022) 399–408, https://doi.org/10.1007/s42757-022-0143-9.

[26] M. Fujioka, L.W. Young, B.R. Girdany, Radiographic evaluation of adenoidal size in children: adenoidal-nasopharyngeal ratio, AJR Am. J. Roentgenol. 133 (1979) 401-404, https://doi.org/10.2214 /ajr.133.3.401.
[27] S. Elwany, The adenoidal-nasopharyngeal ratio (AN ratio). Its validity in selecting children for adenoidectomy, J. Laryngol. Otol. 101 (1987) 569-573, https://doi.org/10.1017/s0022215100102269.
[28] T.O. Adedeji, Y.B. Amusa, A.A. Aremu, Correlation between adenoidal nasopharyngeal ratio and symptoms of enlarged adenoids in children with adenoidal hypertrophy, Afr. J. Paediatr. Surg. 13 (2016) 14-19, https://doi.org/10.4103/0189-6725.181701.
[29] C.M. Hood, R.C. Schroter, D.J. Doorly, E.J.S.M. Blenke, N.S. Tolley, Computational modeling of flow and gas exchange in models of the human maxillary sinus, J. Appl. Physiol. 107 (4) (2009) 1195-1203, https://doi.org/10.1152/japplphysiol.91615.2008.
[30] G. Xiong, J. Zhan, K. Zuo, J. Li, L. Rong, G. Xu, Numerical flow simulation in the post-endoscopic sinus surgery nasal cavity, Med. Biol. Eng. Comput. 46 (11) (2008) 1161-1167, https://doi.org/10.1007/s11517-008-0384-1.
[31] Q.J. Ge, K. Inthavong, J.Y. Tu, Local deposition fractions of ultrafine particles in a human nasal-sinus cavity CFD model, Inhal. Toxicol. 24 (8) (2012) 492-505, https://doi.org/10.3109/0895837 8.2012.694494.
[32] H.O. Coxson, Quantitative computed tomography assessment of airway wall dimensions: current status and potential applications for phenotyping chronic obstructive pulmonary disease, Proc. Am. Thorac. Soc. 5 (2008) 940-945, https://doi.org/10.1513/pats.200806-057QC.
[33] M. Spiegel, T. Redel, Y.J. Zhang, T. Struffert, J. Hornegger, R.G. Grossman, A. Doerfler, C. Karmonik, Tetrahedral vs. polyhedral mesh size evaluation on flow velocity and wall shear stress for cerebral hemodynamic simulation, Comput. Methods Biomech. Biomed. Engin. 14 (2011) 9-22, https://doi.org/10.1080/10255842.2010.518565.
[34] W. Hofmann, Mathematical model for the postnatal growth of the human lung, Respir. Physiol. 49 (1) (1982) 115-129, https://doi.org/10.1016/0034-5687(82)90106-2.
[35] M. Thiriet, Biomathematical and Biomechanical Modeling of the Circulatory and Ventilatory Systems, Springer, New York, 2014.
[36] K.J. Burdach, R.L. Doty, The effects of mouth movements, swallowing, and spitting on retronasal odor perception, Physiol. Behav. 41 (1987) 353-356, https://doi.org/10.1016/0031-9384 (87) 90400-8.
[37] J. Weese, A. Lungu, J. Peters, F.M. Weber, I. Waechter-Stehle, D.R. Hose, CFD- and Bernoulli-based pressure drop estimates: A comparison using patient anatomies from heart and aortic valve segmentation of CT images, Med. Phys. 44 (2017) 2281-2292, https://doi.org/10.1002/mp.1 2203.
[38] Z. Lou, Adenoid hypertrophy in children and allergic rhinitis, Eur. Arch. Otorhinolaryngol. 275 (2018) 831-832, https://doi.org/10.1007/s00405-017-4737-y.
[39] J. Dong, Y. Shang, K. Inthavong, H.K. Chan, J. Tu, Numerical Comparison of Nasal Aerosol Administration Systems for Efficient Nose-to-Brain Drug Delivery, Pharm. Res. 35 (2017), https://doi.org/10.1007/s11095-017-2280-6.
[40] J. Dong, Y. Shang, K. Inthavong, J. Tu, R. Chen, R. Bai, D. Wang, C. Chen, From the Cover: Comparative Numerical Modeling of Inhaled Nanoparticle Deposition in Human and Rat Nasal Cavities, Toxicol. Sci. 152 (2016) 284-296, https://doi.org/10.1093/toxsci/kfw087.

[41] M.A. Fornazieri, R.G. Araujo, J. Lima, F.B. Favareto, F.R. Pinna, R.L. Voegels, R.L. Doty, The effects of adenoidectomy on the smell perception of children, Int. Forum Allergy Rhinol. 9 (2019) 87-92, https://doi.org/10.1002/alr.22209.
[42] G.J. Garcia, J.D. Schroeter, J.S. Kimbell, Olfactory deposition of inhaled nanoparticles in humans, Inhal. Toxicol. 27 (2015) 394-403, https://doi.org/10.3109/08958378.2015.1066904.
[43] D.B. Ingham, Diffusion of aerosols in the entrance region of a smooth cylindrical pipe, J. Aerosol Sci. 22 (3) (1991) 253-257, https://doi.org/10.1016/S0021-8502(05)80003-5.
[44] H. Shi, C. Kleinstreuer, Z. Zhang, Laminar airflow and nanoparticle or vapor deposition in a human nasal cavity model, J. Biomech. Eng. 128 (2006) 697-706, https://doi.org/10.1115/1.2244574.
[45] J. Jiang, K. Zhao, Airflow and nanoparticle deposition in rat nose under various breathing and sniffing conditions-A computational evaluation of the unsteady and turbulent effect, J. Aerosol Sci. 41 (2010) 1030-1043, https://doi.org/10.1016/j.jaerosci.2010.06.005.

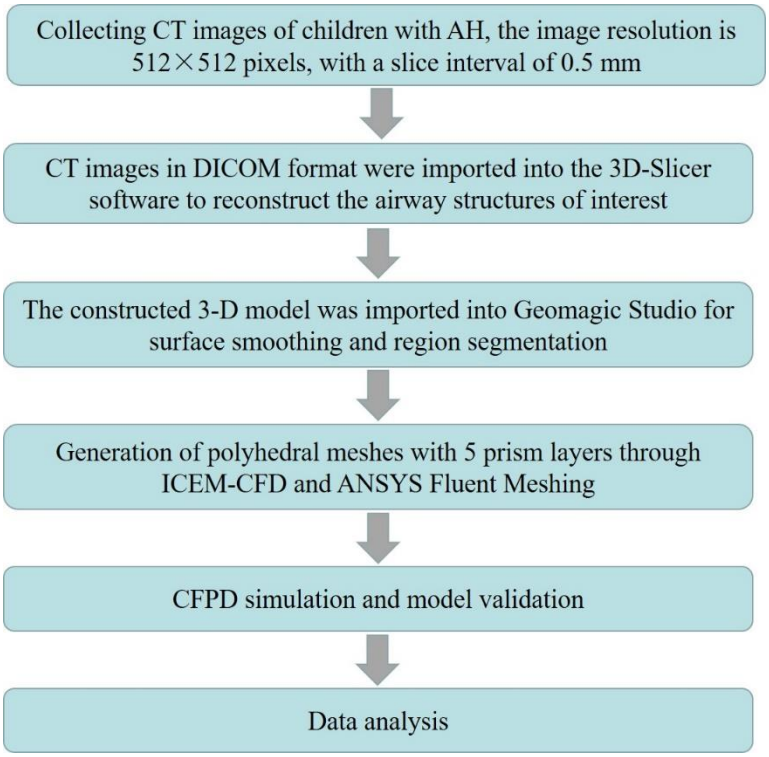

Fig. 1. The specific steps for creating the pediatric nasal cavity model.

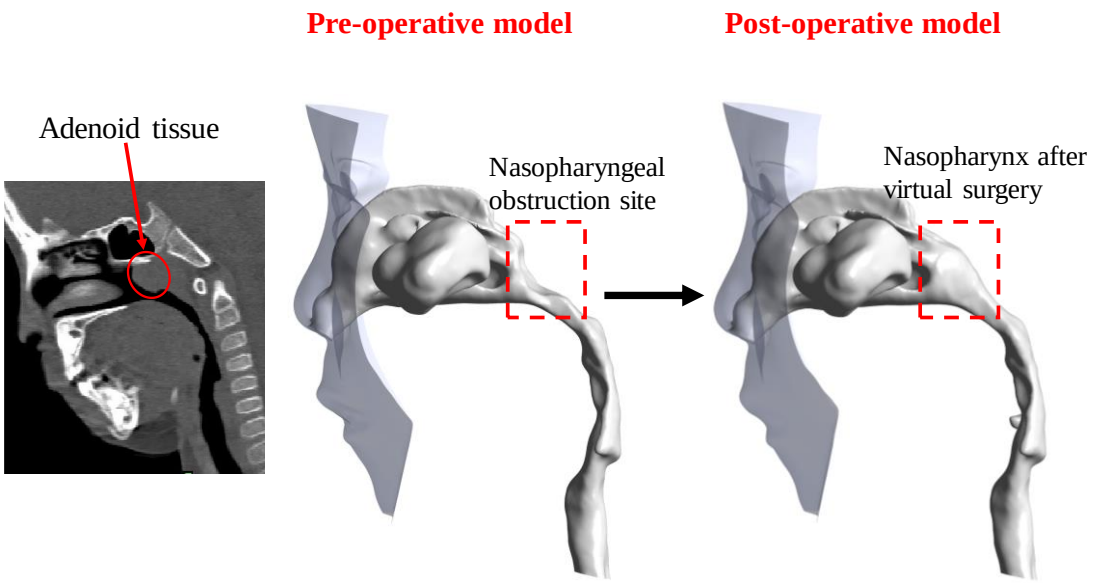

Fig. 2. Pre- and post-operative nasal airway models by virtual surgery to remove the enlarged adenoid tissue.

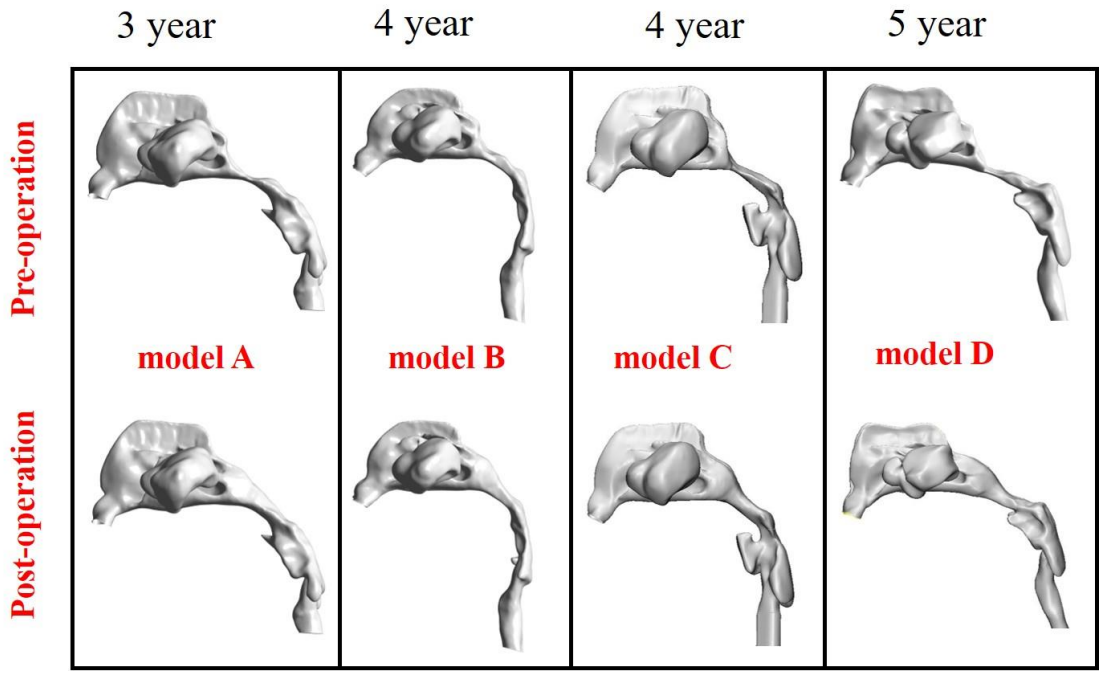

Fig. 3. All pre- and post-operative nasal airway models in this study.

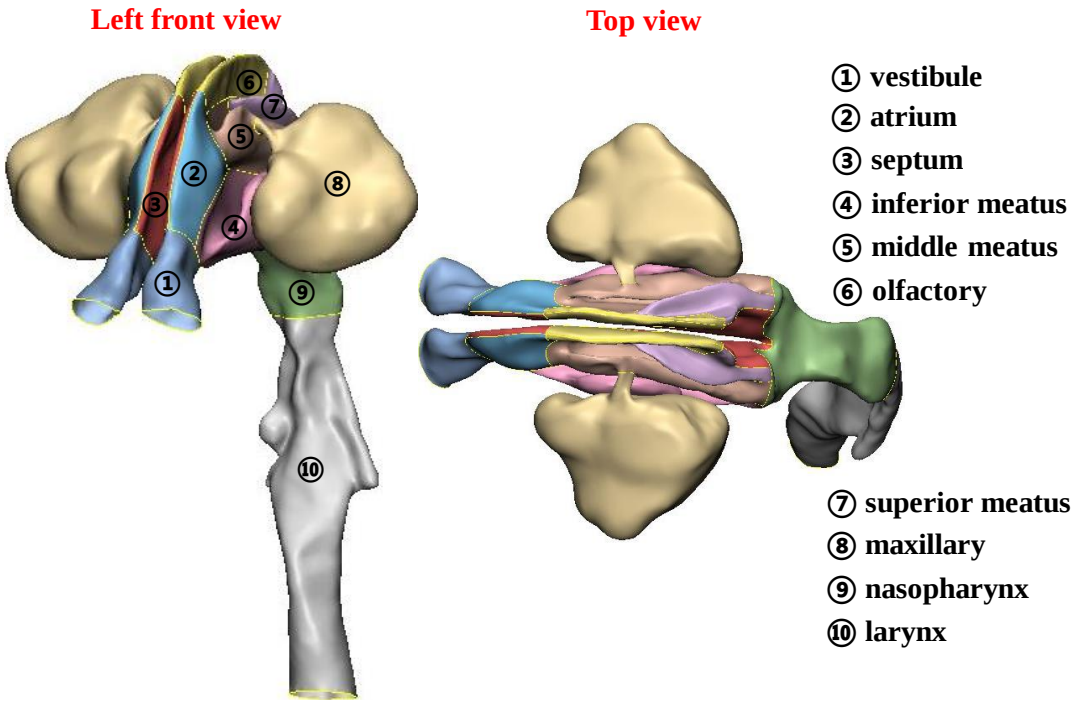

Fig. 4. Diagram of the different anatomical regions of the nasal cavity.

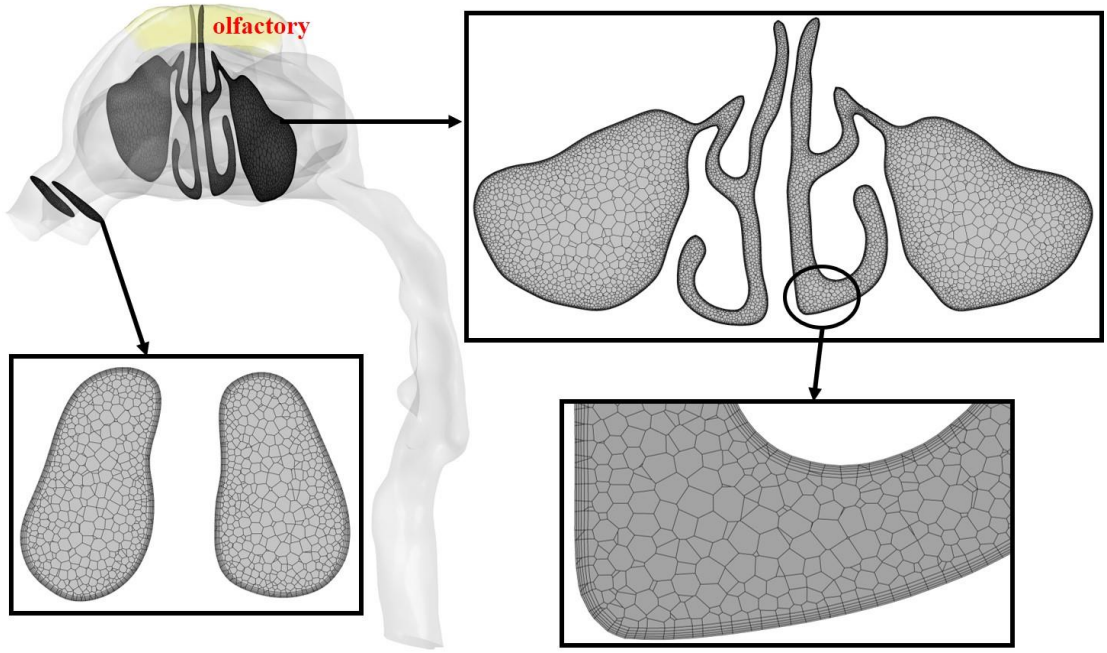

Fig. 5. Cross-sections of mesh showing the polyhedral mesh elements and near wall prism layers. The highlighted region was the targeted olfactory region.

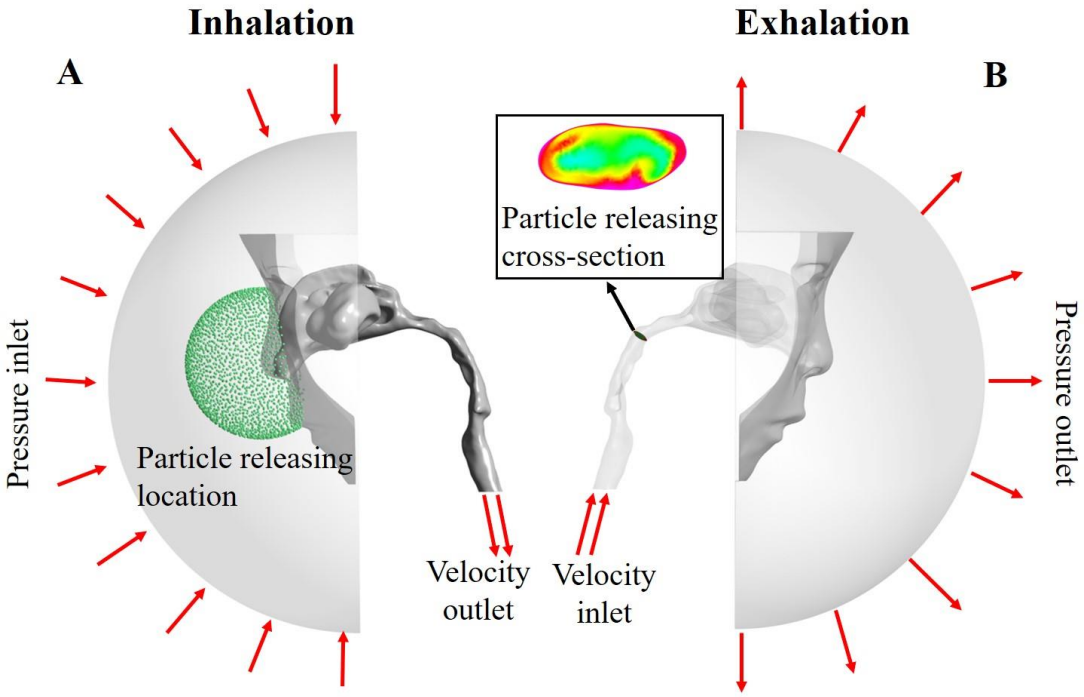

Fig. 6. Boundary conditions for airflow and virtual nanoparticle release during inhalation and exhalation.

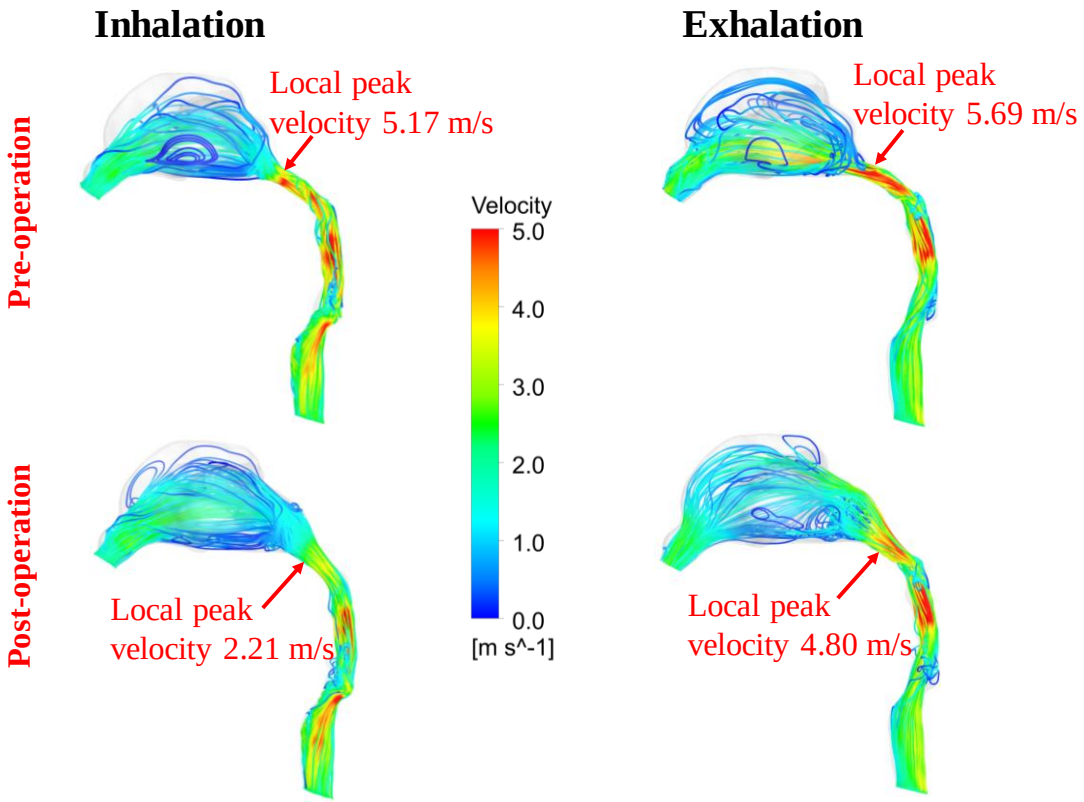

Fig. 7. Airflow streamline distribution in the pre- and post-operative models during inhalation and exhalation. Results are illustrated by using representative model B.

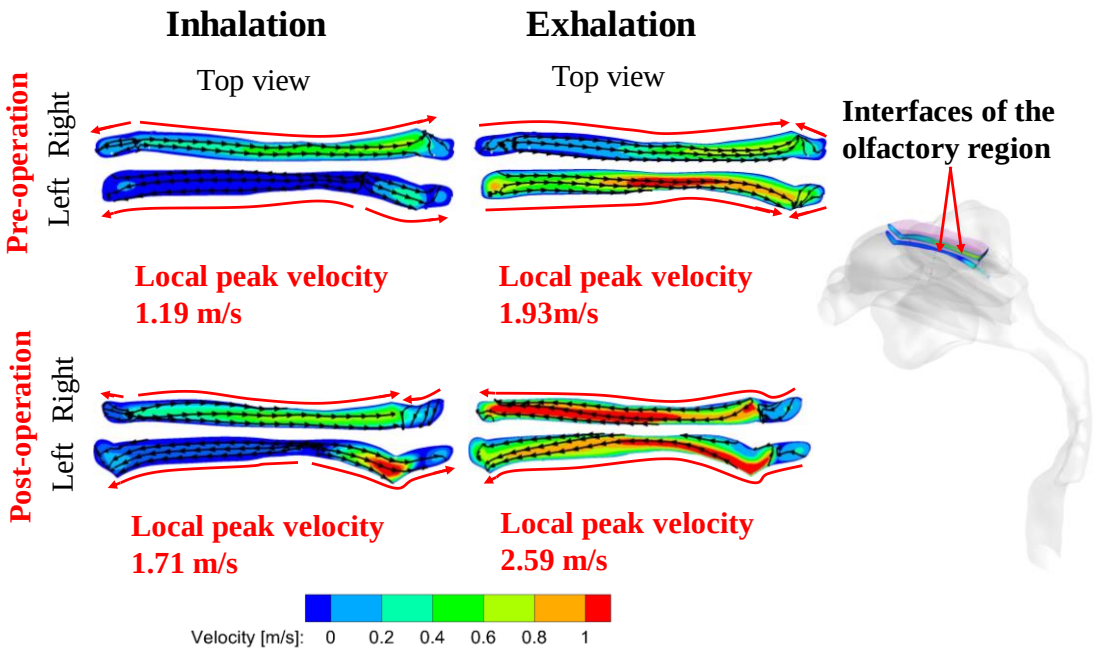

Fig. 8. Ventilation status of the olfactory region in the pre- and post-operative models based on the local velocity distribution at the interfaces of the olfactory region during inhalation and exhalation. Results are illustrated by using representative model B.

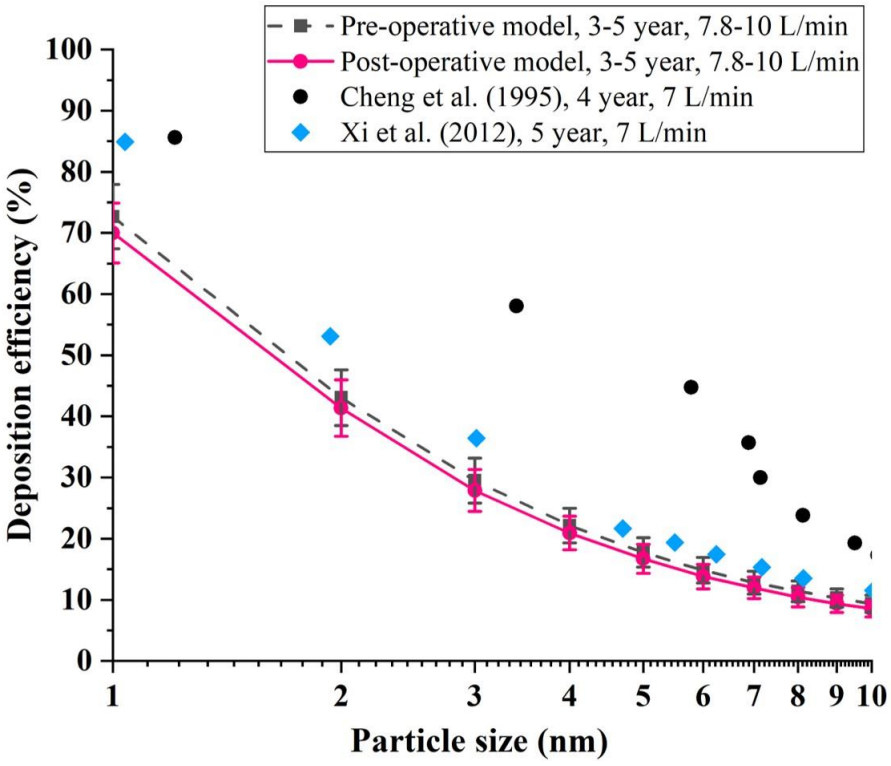

Fig. 9. Mean values (mean ± standard deviation) of nanoparticle DEs for all models in this study, and its comparison with literature data.

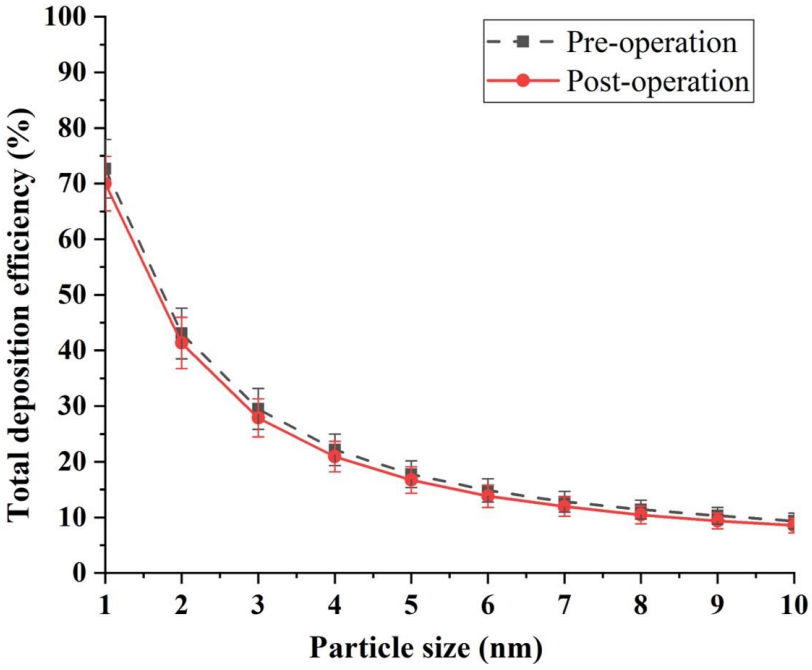

Fig. 10. Comparison of the total DE of nanoparticles in the model before and after surgery during inhalation.

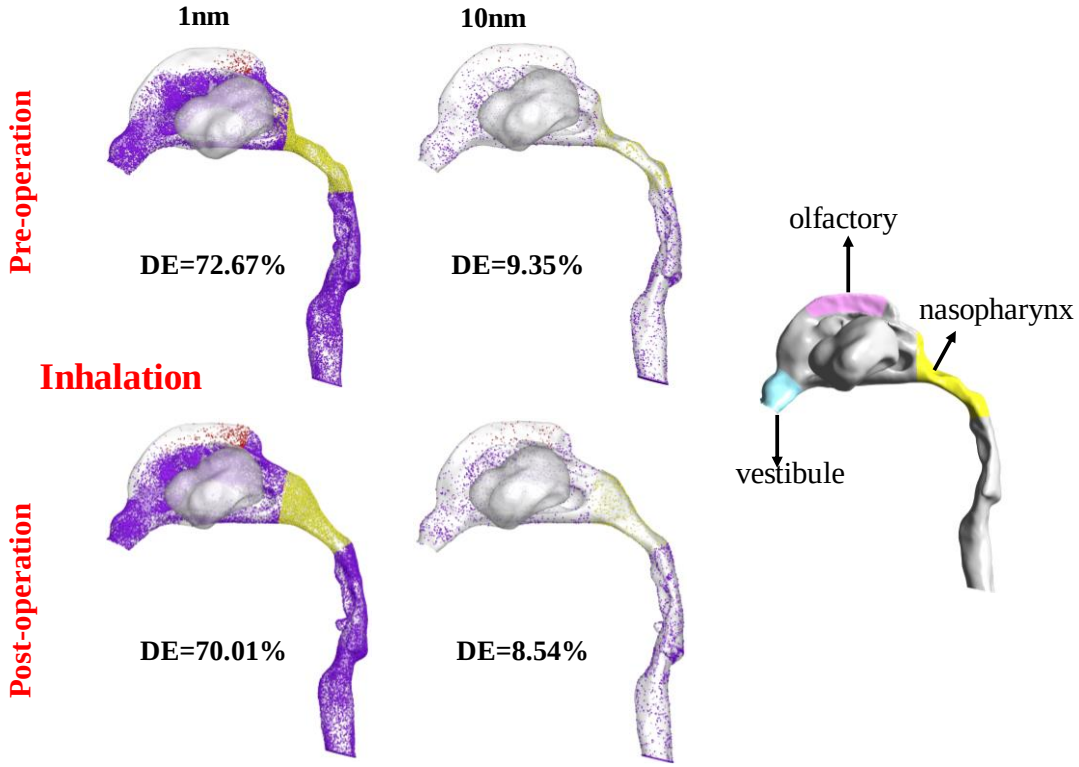

Fig. 11. Spatial deposition patterns of 1 and 10 nm particles in pre- and post-operative models during inhalation. Results are illustrated by using representative model B.

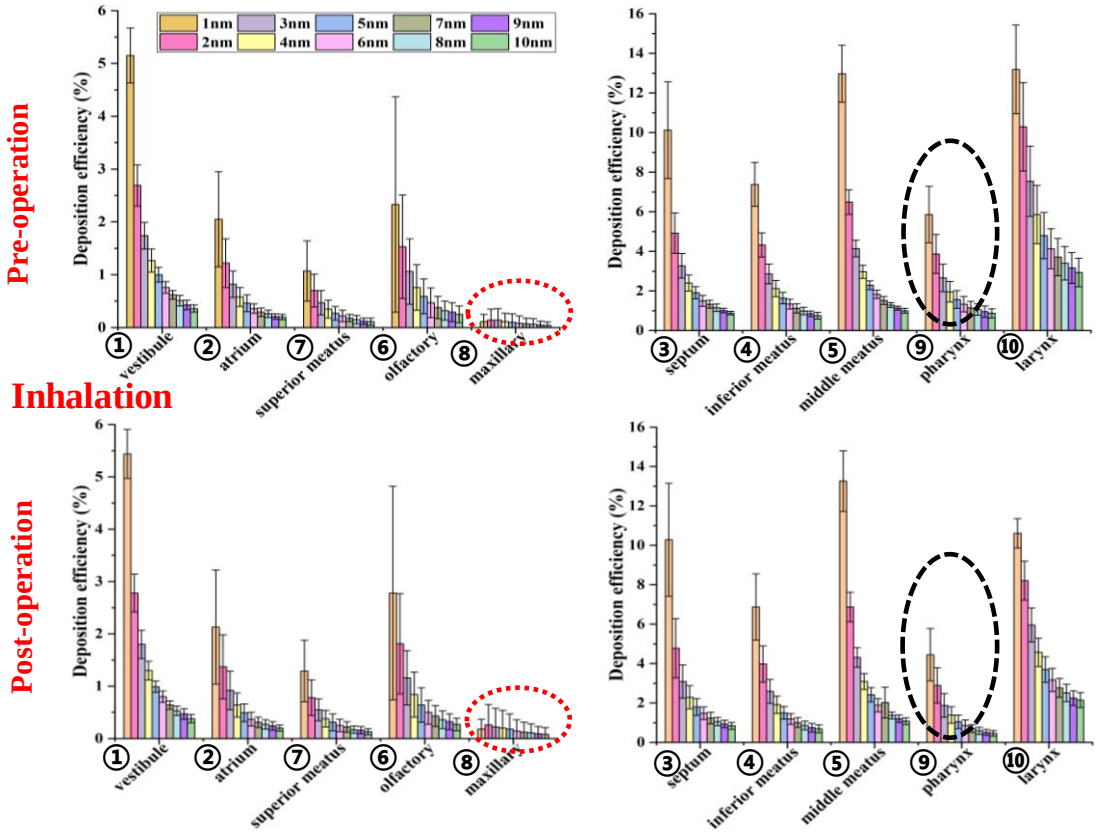

Fig. 12. DEs of nanoparticles at various anatomical sites of the pre- and post-operative models during inhalation.

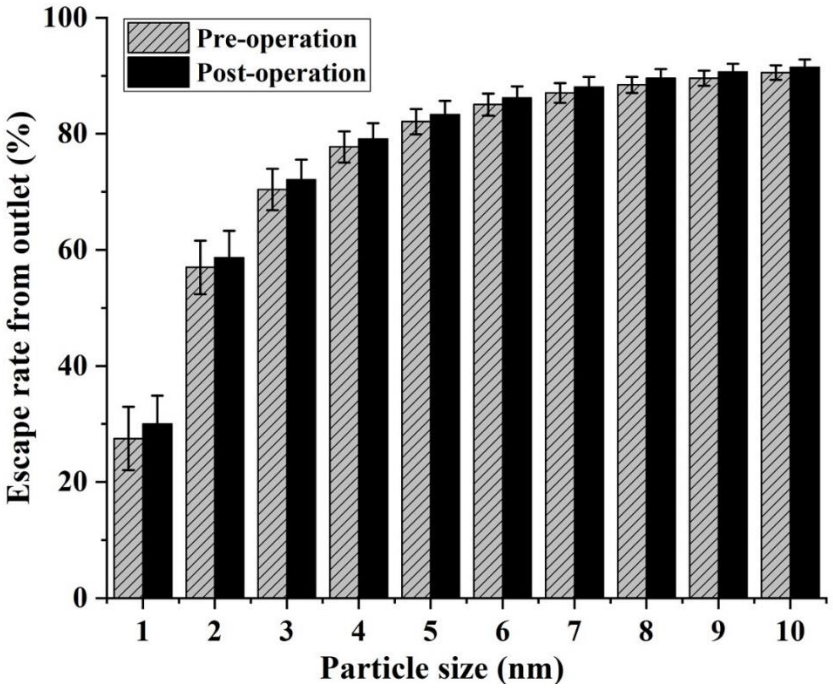

Fig. 13. Escape rate of nanoparticles at the outlet of the model before and after surgery during inhalation.

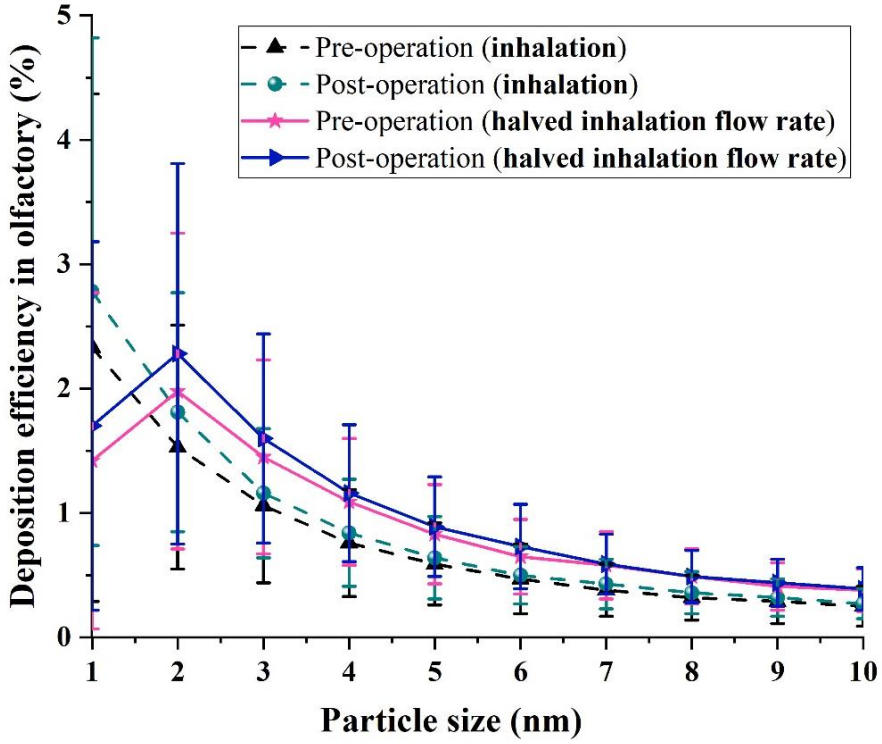

Fig. 14. DEs of nanoparticles in the olfactory region of the model before and after surgery during resting inhalation and when the inhalation flow was halved.

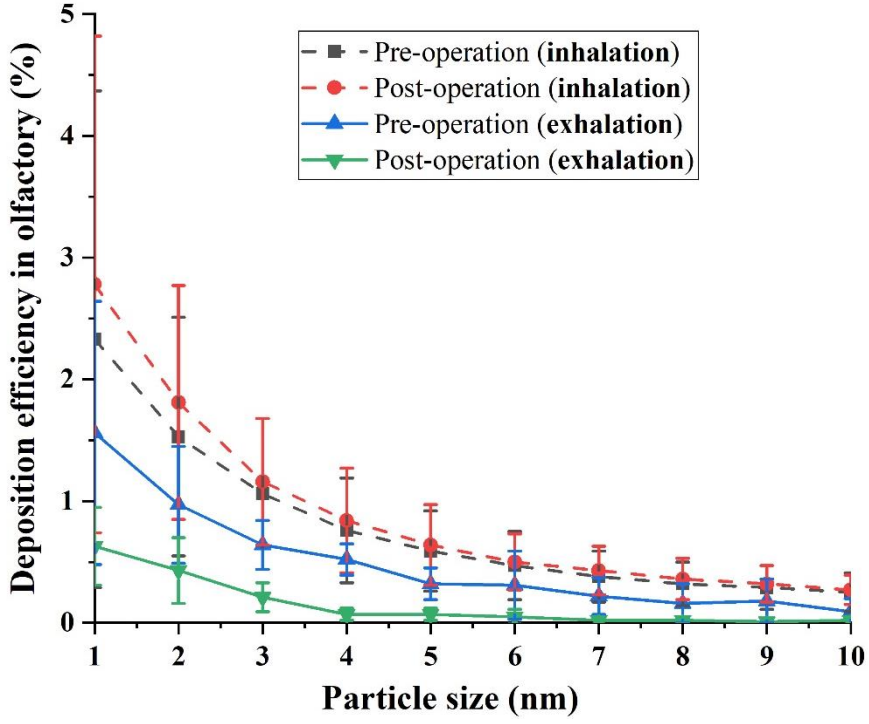

Fig. 15. DEs of nanoparticles in the olfactory region of the model before and after surgery during inhalation and exhalation.

Table 1

Respiratory parameters under quiet breathing conditions.

Age	Tidal volume (mL)	Respiratory rate (breaths/min)	Minute ventilation (mL/min)	Inspiration-to-expiration time ratio	Inhalation flow rate (L/min)
3-Year-Old	121	24	2904	1:1.7	7.84
4-Year-Old	152	22	3344	1:1.7	9.03
5-Year-Old	181	20	3620	1:1.7	9.77

The parameters were obtained from the reference [34,35].